HHS Public Access

Author manuscript

Nat Med. Author manuscript; available in PMC 2016 October 18.

Published in final edited form as:

Nat Med. 2016 May ; 22(5): 497–505. doi:10.1038/nm.4082.

Genotype tunes pancreatic ductal adenocarcinoma tissue tension to induce matricellular-fibrosis and tumor progression

Hanane Laklai[1], **Yekaterina A. Miroshnikova**[1], **Michael W. Pickup**[1], **Eric A. Collisson**[2], **Grace E. Kim**[3], **Alex S. Barrett**[4], **Ryan C. Hill**[4], **Johnathon N. Lakins**[1], **David D. Schlaepfer**[5], **Janna K. Mouw**[1], **Valerie S. LeBleu**[6], **Nilotpal Roy**[7], **Sergey V. Novitskiy**[8], **Julia S. Johansen**[9], **Valeria Poli**[10], **Raghu Kalluri**[6], **Christine A. Iacobuzio-Donahue**[11], **Laura D. Wood**[12], **Matthias Hebrok**[7], **Kirk Hansen**[4], **Harold L. Moses**[8], and **Valerie M. Weaver**[1,13,14,15,16,17]

[1]Center for Bioengineering and Tissue Regeneration, Department of Surgery, University of California, San Francisco, San Francisco, CA, USA

[2]Department of Medicine, University of California, San Francisco, San Francisco, CA, USA

[3]Department of Pathology, University of California, San Francisco, San Francisco, CA, USA

[4]Department of Biochemistry and Molecular Genetics, University of Colorado, Denver, Aurora, CO, USA

[5]Department of Reproductive Medicine, University of California, San Diego Moores Cancer Center, La Jolla, CA, USA

[6]Department of Integrative Biology and Pharmacology, University of Texas Health Science Center at Houston–Medical School, Houston, TX, USA

[7]Diabetes Center, Department of Medicine, University of California, San Francisco, CA USA

[8]Department of Cancer Biology, Vanderbilt University School of Medicine, Nashville, TN, USA

[9]Department of Oncology, Herlev Hospital, Copenhagen University Hospital, Copenhagen, Denmark

[17]Correspondence to: Valerie M. Weaver, San Francisco, CA 94143, ; Email: Valerie.Weaver@ucsf.edu

Author Contributions

V.M.W. and H.L. conceived the project. H.L. designed and conducted transgenic mice experiments and treatments, performed histology, immunofluorescence and image analysis on mice and human samples, fabricated and conducted experiments with the PA hydrogels, performed 3D collagen and soft agar assays, performed the cytokine array and analysis, and performed the immunoblotting analyses. H.L. and Y.A.M. performed AFM imaging and analysis. Y.A.M. performed TFM and two-photon imaging and analysis. H.L. and M.W.P. conducted orthotopic xenografts experiments. M.W.P performed RT-PCR and bioinformatics. S.V.N. and M.W.P. performed flow sorting. J.N.L designed and constructed expression constructs and the V737N transgenic mouse. E.A.C. and G.E.K. aided with pathological pancreatic cancer scoring of transgenic mice and human samples. J.S.J. and E.A.C. collected human samples from short and long survival patients and aided in the interpretation of the data. C.A.I-D and L.D.W collected human samples from wild type and mutant SMAD4 patients and aided in the interpretation of the data. R.K., V.S.L, M.H and N.R. provided KPC pancreatic tissues. V.P. provided $Stat3^{flox/flox}$ and constitutively active Stat3C transgenic mice. A.S.B., R.C.H and K.H. performed LC-MS/MS and LC-SRM Proteomic analysis. D.D.S provided FAK inhibitor PND-1186.H.L.M designed and provided KTC transgenic mouse, provided KC mice and aided in interpretation of data. V.M.W., H.L, Y.A.M., J.K.M and M.W.P wrote the manuscript with input from all authors.

Competing Financial Interests

We currently have no competing financial interests to report.

[10]Department of Molecular Biotechnology and Health Sciences, Molecular Biotechnology Center, University of Turin, Turin, Italy

[11]Department of Pathology, David Rubenstein Center for Pancreatic Cancer Research, Human Oncology and Pathogenesis Program, Memorial Sloan Kettering Cancer Center, New York, New York, USA

[12]Gastrointestinal and Liver Pathology Department, Johns Hopkins University, Baltimore, MD, USA

[13]Department of Anatomy, University of California, San Francisco, San Francisco, CA, USA

[14]Department of Bioengineering and Therapeutic Sciences, University of California, San Francisco, San Francisco, CA, USA

[15]Eli and Edythe Broad Center of Regeneration Medicine and Stem Cell Research, University of California, San Francisco, San Francisco, CA, USA

[16]Helen Diller Comprehensive Cancer Center, University of California, San Francisco, San Francisco, CA, USA

Abstract

Fibrosis compromises pancreatic ductal carcinoma (PDAC) treatment and contributes to patient mortality yet anti-stromal therapies are controversial. We found that human PDACs with impaired epithelial transforming growth factor β (TGF-β) signaling have elevated epithelial Stat3 activity and develop a stiffer, matricellular-enriched fibrosis associated with high epithelial tension and shorter patient survival. In several Kras-driven mouse models, both the loss of TGF-β signaling and elevated β1-integrin mechanosignaling engaged a positive feedback loop whereby Stat3 signaling promotes tumor progression by increasing matricellular fibrosis and tissue tension. In contrast, epithelial Stat3 ablation attenuated tumor progression by reducing the stromal stiffening and epithelial contractility induced by loss of TGF-β signaling. In PDAC patient biopsies, higher matricellular protein and activated Stat3 associated with SMAD4 mutation and shorter survival. The findings implicate epithelial tension and matricellular fibrosis in the aggressiveness of SMAD4 mutant pancreatic tumors, and highlight Stat3 and mechanics as key drivers of this phenotype.

Introduction

PDAC fibrosis compromises drug delivery, impedes immune cell accessibility and promotes disease aggression and therapy resistance[1–4]. To this end, inhibition of stromal sonic hedgehog (SHH) signaling in a mouse model significantly reduced fibrosis and increased drug update that, at least transiently, stabilized the disease[5]. Similarly, reducing the abundance of mouse tumor hyaluronan, using hyaluronidase, or treating xenografted human pancreatic tumors with an angiotensin inhibitor to reduce tissue tension, decreased facilitated chemotherapy delivery[1,6]. Yet, phase II clinical trials targeting fibrosis failed to increase patient survival[7]. Experiments in mouse models of PDAC revealed that, while depletion of proliferating α-smooth muscle actin (α-SMA) positive stromal cells reduced fibrosis, the vasculature remained abnormal and the tumors were hypoxic and less

differentiated, resulting in accelerated mortality[8]. Additionally, despite a reduction in fibrosis and enhancement of tissue vascularity, genetic ablation of SHH or treatment with a smoothened inhibitor resulted in mouse PDACs that were less differentiated and more aggressive[9].

At first glance, these data imply that the stroma can both promote and restrain tumor progression and suggest stromal dependency may be context dependent. Nevertheless, underlying assumptions informing these experimental and clinical manipulations were similarities in tissue across all PDACs regardless of tumor genotype, the mediation of stromal remodeling in PDACs by a uniform population of stromal fibroblasts, and a comparable physical impact of fibrosis including the restraint of the tumor cells, the impedance of tumor-associated vasculature and the prevention of immune infiltratation[10–12]. Yet the extent, nature and tumor cell response to the of tumor-associated fibrosis varies widely across cancers, tumor subtypes and even within the same tumor and the stromal population that contributes to ECM deposition and remodeling in tumors is heterogeneous[13–16]. Importantly, oncogenic transformation itself increases tumor cell tension that can critically contribute to ECM remodeling and the malignant phenotype as was demonstrated by a ras-transformed epithelium whose ROCK-dependent contractility and fibrosis induction was essential for Wnt-dependent squamous carcinoma progression[17–19]. Clearly sorting out the contribution of stromal and epithelial elements to PDAC fibrosis and pathology would go far to guide the development and application of anti-stromal therapies.

Patients whose tumors harbor Mothers Against DPP Homolog 4 (SMAD4) mutations die more frequently from disseminated disease[20], and reduced levels of epithelial Smad4 enhanced the aggressiveness and increased dissemination of tumor cells from the PDACs that developed in an experimental mouse model[21]. Interestingly, experimental tumors with combined Kras mutations and Tgfbr2 deletion are highly fibrotic and exhibit a pronounced mesenchymal-like phenotype following stromal ablation[8,22]. Clinically, patient PDACs with a quasi-mesenchymal phenotype are more aggressive and treatment-resistant as compared to PDACs with a classical, more-differentiated histophenotype[23,24]. Moreover, the mesenchymal-like patient PDACs often associate with aberrant TGF-β signaling in the epithelium[25]. These findings suggest that PDACs in which TGF-β signaling is compromised may have a unique stromal-epithelial interaction phenotype that could influence their response to anti-stromal therapies. As such, we investigated the interplay between tumor genotype and fibrotic phenotype in PDAC progression.

Results

Tissue tension and collagen thickness linked to PDAC prognosis

Fibrillar collagen has been implicated in PDAC aggression and treatment resistance[26], yet recent findings suggest collagen abundance in PDAC may associate with better, not worse, patient prognosis and with a more differentiated PDAC phenotype[27–29]. We constructed a gene list of major fibrillar collagens (Supplementary Table 1) and used this signature to stratify publically-available NCBI GEO data. We found no significant association between the levels of the major fibrillar collagens and patient survival. However, when we stratified

patient data for high versus low Col1α2, Col2α1 and Col4α1 expression, patients expressing high levels of these specific collagens had a reduced overall survival (log rank $p \leq 0.04$; Supplementary Fig. 1a).

To investigate the relationship between fibrillar collagen and PDAC phenotype, we assessed total and fibrillar collagen in PDAC tissue arrays with well ($n = 19$), moderately ($n = 23$) and poorly differentiated ($n = 26$) tumors. Although total and fibrillar collagens were similar in all tumor biopsies regardless of differentiation status (Fig. 1a;Supplementary Fig. 1b, c), we noted a reduction in the number of alpha smooth muscle actin α-SMA) positive cells in the poorly differentiated PDAC tumor biopsies, as compared to the well and moderately differentiated tumors (Fig. 1a; $p \leq 0.05$)[8,30]. Moreover, the diameter of the collagen fibers adjacent to the epithelial lesions was significantly thicker in the poorly differentiated PDACs (Fig. 1; $p \leq 0.01–0.001$). We also detected a progressive increase in level of phosphorylated myosin light chain 2 (pMLC2) in the epithelium that was adjacent to the thicker collagen fibers in the moderately and poorly differentiated tumors, consistent with increased epithelial actomyosin tension (Fig. 1a; $p \leq 0.05–0.001$) suggesting an association may exist between tumor cell tension and the architecture of the adjacent collagen bundles[1931].

To investigate the relationship between fibrillar collagen, epithelial tension and patient survival, we stratified PDAC tumors from a cohort of patients[32] by survival (median survival <10 months versus median survival >24 months). Again, we found no association between total and fibrillar collagen or α-SMA-positive cells to patient survival (Fig. 1b, Supplementary Fig. 1d,e). However, the diameter of the collagen fibers adjacent to the pancreatic lesions was significantly thicker in patients with the shortest survival (Fig. 1b; $p \leq 0.001$). We also observed elevated pMLC2 in the PDAC tissues from patients with the shortest survival, indicating increased actomyosin tension and a relationship between the contractile PDAC epithelium and the reorganized collagen bundles (Fig. 1b; $p \leq 0.001$).

TGF-β signaling is often attenuated in patient PDACs[33], thus we assessed phosphorylation of SMAD2 as a primary mediator of canonical TGF-β signaling. The least differentiated PDAC lesions (Fig. 1a; $p \leq 0.001$) and the PDACs derived from the patients with the shortest survival (Fig. 1b; $p \leq 0.001$) had less detectable pSMAD2, suggesting they had compromised TGF-β signaling[34,35]. Next, we compared the stromal phenotype of patient PDACs with genetically altered SMAD4 to PDACs with wild type SMAD4[36]. While total collagen and α-SMA levels were similar between both cohorts (Supplementary Fig. 1f), we observed elevated epithelial pMLC2 (Fig. 1c; $p \leq 0.001$) with increased adjacent collagen fibers in PDACs lacking functional SMAD4 (Fig. 1c; $p \leq 0.001$). Atomic Force Microscopy (AFM) mechanical testing revealed that the thickened, epithelial-adjacent collagen fibers were stiffer in the PDACs from patients whose lesions lacked a functional SMAD4 (Fig. 1c; $p \leq 0.001$). These findings indicate that the architecture and mechanics of collagen fibers adjacent to the epithelial lesion, and not bulk collagen abundance, may be an indicator of PDAC aggression and that a reduction in TGF-β signaling in the PDAC epithelium may influence the nature of the stromal response.

PDAC genotype tunes epithelial tension to regulate fibrosis

To explore the relationship between TGF-β signaling, collagen organization and tissue mechanics, we exploited available PDAC genetically-engineered mouse models (GEMMs). By 20 weeks KC (*Kras*$^{LSL\text{-}G12D/+}$*Ptf1α*-Cre)[37] mice had progressed to PanIN lesions, whereas the KPC (KC with mutant *Tp53*$^{+/-}$; *Kras*$^{LSL\text{-}G12D/+}$*Tp53*$^{R172H/+}$*Pdx1*-Cre) and KTC (KC with *Tgfbr2*$^{flox/wt}$; *Kras*$^{LSL\text{-}G12D/+}$*Tgfbr2*$^{flox/wt}$*Ptf1a*-Cre) mice developed PDAC lesions[22,38]. Coincident with tumor formation, the pancreatic tissues of both the KPC and KTC mice were highly fibrotic, indicated by abundant quantities of total and fibrillar collagen (not shown). Targeted proteomics confirmed that many of the fibrillar collagens in the KTC and KPC mice were present at similar levels (Supplementary Table 2). Immunofluorescence staining showed that KTC and KPC tumors had similar stromal levels of collagen III, α-Sma and fibroblast activated protein (Fap) (Supplementary Fig. 2a). GLI family zinc finger 1 (Gli1), which regulates PDAC fibrosis, was abundantly and uniformly expressed in the KPC and KTC tumor stroma (Supplementary Fig. 2a). Nevertheless, and in agreement with our clinical findings, KTC PDAC lesions had thicker collagen bundles and a stiffer ECM in the periductal region (Fig. 2a–c; $p \leq 0.001$). Mass spectrometry and immunofluorescence analyses of the tumor ECM further revealed that the altered fibrillar collagen phenotype and the elevated ECM stiffness in the KTC PDAC lesions was accompanied by a significant increase in tenascin C, fibronectin and collagen, type XII, alpha 1 (Supplementary Fig. 3b, $p \leq 0.05$; Table 2; Fig 2a–b, $p \leq 0.01$–0.001). The KTC PDAC epithelium was also more contractile as indicated by more pMLC2 and myosin phosphatase target subunit 1 (p-MyPT1; Fig 2a, Supplementary Fig 3a; $p \leq 0.01$–$0,001$) and higher mechanosignaling indicated by activated β1-integrin, phosphorylated focal adhesion kinase (^{p397}-Ptk2; Fig. 2a, Supplementary Fig. 3a; $p \leq 0.05$–0.01) and nuclear Yorkie activated protein (YAP1; Fig. 2a, Supplementary Fig. 3a; $p \leq 0.01$–0.001;[39]). These data suggest that a reduction in TGF-β signaling increases actomyosin tension and mechanosignaling in a transformed pancreatic epithelium to induce a stiffer, periductal, matricellular-enriched fibrosis.

We next assessed the contractility phenotype of individual PDAC epithelial cells derived from KC, KTC and KPC mice using traction force microscopy (TFM). KTC tumor cells were more than the KPC or KC cells (Supplementary Fig. 3c). The KTC tumor cells promoted more Rho kinase 1 (Rock1) and not Rock 2-dependent 3D collagen gel contraction than KPC or KC mouse tumor cancer cells (Supplementary Fig. 4a; $p \leq 0.01$–0.001). (Fig. 2d; $p \leq 0.01$–0.001; Supplementary Fig. 5a–d). The KTC tumor cells exhibited higher Rock1 dependent tumor growth (Fig. 2g, Supplementary Fig. 4d). Myosin tension, as revealed by elevated traction force as well as pMLC2 (Fig 2e, Supplementary Fig. 4c), induced more nuclear Yap1 and YAP activity as indicated by higher *Ctgf* (Fig. 2e, Supplementary Fig. 4c) and promoted a greater fiber diameter (Fig. 2f; $p \leq 0.001$) that was stiffer and enriched for the matricellular protein tenascin C (Fig. 2g–i; $p \leq 0.01$–0.001) upon orthotopic injection into the pancreas of immune-compromised mice. These data demonstrate that a reduction of TGF-β signaling in the pancreatic epithelium increases tumor cell tension to induce a stiffer, matricellular fibrosis.

KTC tumor cells also showed a significant increase in anchorage-independent growth and colony formation (Supplementary Fig. 4f; $p \leq 0.05–0.001$) which is consistent with a reduced dependence on ECM ligation for tumor cell survival and the enhanced metastasis incidence observed in patients with mutant SMAD4[40,41]. However, the size of the KTC tumors was significantly smaller than those formed by KPC cells (Supplementary Fig. 4d–e). Thus, although pancreatic transformation is universally accompanied by a progressive fibrosis and stiffening of the ECM, the nature of the fibrotic response and the mechano-phenotype of the cancer can be modified by the genotype of the tumor.

JAK-Stat3 signaling drives ECM remodeling and stiffening

We next sought to clarify how reduced TGF-β signaling could increase tumor cell tension. G protein coupled receptor (GPCR)-mediated Janus kinase (Jak) activation stimulates activation of both signal transducer and activator of transcription 3 (Stat3) and ROCK, and induces actomyosin-mediated cell contractility and Stat3 has been implicated in PDACs[4243_46]. We noted that pStat3 staining was significantly higher in the pancreatic epithelium of the KTC mice compared to KPC or KC mice (Fig. 3a; $p \leq 0.001$), even in the eight week old PanINs where the amount of infiltrating immune cells is quite low (Supplementary Fig. 6a; $p \leq 0.001$). Although both the stroma and the PDACs in the KPC and KTC mice stained positively for pStat3, coincident with an abundant immune infiltrate[46], pStat3 was significantly higher only in the tumor pancreatic epithelium in KTC mice (Fig. 3a; $p \leq 0.001$). We also detected abundant pStat3 *in vitro* in non-stimulated KTC, but not KPC or KC, cells (Fig. 3b, Supplementary Fig 5a). KTC tumor cell contraction and remodeling of collagen gels was blocked by treatment with the JAK inhibitor Ruxolitinib (Fig. 3c,d, Supplementary Fig. 6b). We also noted that the 48 hour conditioned media from KTC tumor cells activated pStat3 in cultured KC cells (Fig. 3e), and simultaneously increased the JAK-dependent ability of the KC cells to contract and remodel collagen gels (Fig. 3g; $p \leq 0.0.001–05$; Supplementary Fig. 6c). A stiff ECM can enhance Stat3 activation[47], and we observed higher steady state pStat3 levels in KC tumor cells and higher levels of secreted cytokines in the media of Kras pancreatic tumor cells when they were plated on a stiff ECM (Fig. 3f,i, $p \leq 0.01$; Fig. 3g, $p \leq 0.05–0.001$; Supplementary Fig. 6d–f). These findings identify an epithelial Jak-Rock-Stat3 signaling circuit as a candidate KTC tumor cell-specific contractility mechanism that could induce ECM remodeling and foster the development of a matricellular-enriched pancreatic fibrosis.

Tumor cell tension accelerates PDAC progression in mice

To test links between pStat3, tumor tension and fibrosis in PDAC progression we crossed transgenic mice expressing *Ptf1a*-Cre with mice expressing a conditional V737N β1-integrin (Supplementary Fig. 7a), which recapitulates tension-dependent integrin clustering and promotes focal adhesion signaling and ROCK-dependent cell contractility in the pancreatic epithelium[18,48,49]. Immunofluorescence staining for confirmed elevated Ptk2 activity ($p \leq 0.001$) in the pancreatic epithelium in the β1–V737N mice, and revealed higher epithelial contractility as indicated by increased pMlc2 ($p \leq 0.001$) and higher mechanosignaling as indicated by nuclear localization of Yap targets including *Ctgf* ($p \leq 0.05$; Supplementary Fig. 7b–c). Evidence of fibrosis was indicated by increased picrosirius red (PR) staining (Supplementary Fig. 7b) and second harmonic generation (SHG) revealed thicker, denser

collagens (not shown); AFM mechanical testing showed a significant stiffening of the ECM surrounding the ductal epithelium (Supplementary Fig. 7b). The presence of pStat3-positive pancreatic epithelial cells in the β1-V737N mice ($p \leq 0.05$), even in the absence of any activating oncogene or pre-existing inflammation, confirmed that epithelial tension can directly enhance Stat3 activation, altered cytokine expression, and immune cell infiltration (Supplementary Fig. 7b–e). Consistently, treatment of the β1-V737N mice with a FAK inhibitor reduced pStat3, ^{p397}FAK, and pMLC2 abundance as well as the matricellular-enriched fibrosis (Supplementary Fig. 8a). Orthotopic injection of KTC cells expressing an shRNA against FAK (Supplementary Fig. 9a,b) into immunocompromised mice also reduced fibrosis ($p \leq 0.001$), decreased stiffness ($p \leq 0.01$) and lowered tenascin C levels ($p \leq 0.001$) towards that of control tumors. The pancreatic tumor epithelium expressing the *Ptk2* shRNA was less mechanically-activated, as indicated by reduced nuclear Yap1 ($p \leq 0.001$), and had reduced levels of nuclear pStat3 ($p \leq 0.001$; Fig. 4e), than control tumors.

To assess the relationship between epithelial tension and PDAC development, we bred *Ptf1α*-Cre V737N β1-integrin mice with KC mice (Fig. 4a) and found that, at 5 weeks of age, the pancreatic epithelium in the KC mice expressing the β1-V737N transgene had significantly higher ^{p397}Ptk2 ($p \leq 0.001$) and pMlc2 ($p \leq 0.01$). The amount and distribution of collagen fibers and ECM stiffness were highest in the periductal region (Fig. 4b; $p \leq 0.001$), similar to what we observed in the developing KTC lesions (compare SHG in Fig. 2a to PS in Fig. 4b). Consistent with the matricellular-enriched fibrosis observed in both the patient samples lacking pSmad and the PDAC lesions in the KTC mice, we detected abundant tenascin C and higher levels of epithelial pStat3 in the KC/β1-V737N tumors (Fig. 4b; $p \leq 0.001$). This phenotype was accompanied by an increase in infiltrating CD68 macrophages (Fig. 4b; $p \leq 0.05$), and FACS characterization of the immune cell population revealed an increase in CD45+/CD11b myeloid cells and CD45+/Ly6C monocytes (Supplementary Fig. 9d). Indeed, cytokine array analysis demonstrated that the KC/β1-V737N mouse pancreas expressed higher levels of pro-inflammatory factors C5α and IL1 (Supplementary Fig. 9e). KC/β1-V737N mice developed chronic pancreatitis as early as 3 months of age (Fig. 4c). Alcian blue staining of the 3 month old KC/V737N mouse pancreatic tissue revealed that the lesions had progressed to advanced, high grade PanINs and that these foci were evenly distributed throughout the tissue. 38% of the KC/β1-V737N animals developed frank PDAC by 5-8 months of age, with accompanying physiological trauma, including loss of body weight (Fig. 4d, Supplementary Fig. 9c). These results reveal that increasing the cytoskeletal contractility in pancreatic tumor cells drives remodeling and stiffening of the periductal ECM, induces a matricellular-enriched fibrosis and promotes pancreatic transformation.

Stat3 induces fibrosis and accelerates PDAC

We next explored the relationship between Stat3 activation, cell contractility and a pancreatic matricellular-enriched fibrosis in PDAC. We crossed KC mice to mice expressing one allele of a constitutively-active Stat3[50] (Stat3C, Fig. 5a). Stat3C mice contained significantly more cells within the pancreas that stained positively for activated Stat3 (Supplementary Fig. 11a; $p \leq 0.001$) and the level of pStat3 was further increased after expression of activated Kras (Fig. 5b; $p \leq 0.001$). We quantified higher numbers of CD45+

immune cells ($p \leq 0.001$) and CD68+ macrophages ($p \leq 0.05$) within the Stat3C pancreatic tissues (Supplementary Fig. 11a); these immune infiltrate further increased with Kras activation (Fig. 5b; $p \leq 0.05$–0.001). Indeed, the pancreatic tissues of the Stat3C/Kras mice showed marked pancreatitis that developed into frank PDAC, and shortened survival compared to Kras mice (Fig. 5c). Consistent with a link between Stat3 and ROCK, although tumors were stiffer and pMLC2 was abundant in the KC/Stat3C mice, pMLC2 levels were already elevated significantly ($p \leq 0.001$) in the pancreatic tissues of the Stat3C mice, even in the absence of Kras (Fig. 5b, 5d, Supplementary Fig. 11a). The pancreas of the Stat3C mice contained abundant mature type I collagen (Supplementary Fig. 11a; $p \leq 0.005$) and elevated ^{p397}Ptk2 throughout (Supplementary Fig. 11a; $p \leq 0.05$). These findings link Stat3 activation and tissue inflammation, and suggest that pStat3 induces ROCK-dependent ECM remodeling and stiffening to drive fibrosis and elevate mechanosignaling in PDACs.

To establish a causal relationship between Stat3 activation, tissue mechanics and a matricellular-enriched fibrosis and PDAC development, we crossed mice expressing Kras and homozygous for loss of both Tgfbr2 alleles[21] (KTC KO; $Kras^{LSL\text{-}G12D/+}Tgfbr2^{flox/flox}$), which exhibit an accelerated matricellular-enriched fibrotic phenotype and PDAC development (Supplementary Fig. 10a–c) and mice expressing a conditional Stat3 knockout[51] in the pancreatic epithelium (Stat3 KO; $Stat3^{flox/flox}$Ptf1α-Cre) to create KTC KO/Stat3 KO mice (Fig. 5e). Immunostaining confirmed deletion of Stat3 in the pancreatic epithelium (Fig. 5f; $p \leq 0.001$) accompanied by significantly reduced CD68+ cell tissue infiltration ($p \leq 0.001$), consistent with decreased inflammation (Fig. 5f). Loss of epithelial Stat3 was also accompanied by a significant reduction in epithelial ^{p397}Ptk2, pMlc2 and nuclear Yap1 levels ($p \leq 0.001$) as well as Yap transcriptional activity as indicated by significantly lower *Ctgf* expression (Fig. 5f, Supplementary Fig. 9b; $p \leq 0.05$). Also, pancreatic tissues with deleted epithelial Stat3 showed a significant reduction in a matricellular-rich fibrosis and ECM stiffness ($p \leq 0.001$), along with a significant increase in mouse survival (Fig. 5f–h).

Direct links between a matricellular-rich fibrotic phenotype, mechanics and pStat3 were confirmed in a cohort of KTC mice treated with the JAK inhibitor Ruxolitinib. Ruxolitinib treatment inhibited pStat3 activity and significantly reduced ^{p397}Ptk2, pMlc2, collagen fibrillogenesis, matricellular matrix enrichment and ECM stiffening (Supplementary Fig. 11c–d; $p \leq 0.01$–0.001) as well as Yap activation (not shown). Moreover, in the absence of JAK-driven matricellular-rich fibrosis, mechanosignaling, Stat3-dependent inflammation and PDAC development were significantly reduced (Supplementary Fig. 11c, 11e; $p \leq 0.01$–0.001).

We investigated the clinical relevance of STAT3 activation in matricellular-enriched fibrosis and PDAC progression, and found elevated levels of tenascin C, fibronectin and collagen 12 ($p \leq 0.05$), high nuclear YAP1 ($p \leq 0.05$) (Fig. 6a) and elevated SOX2, vimentin ($p \leq 0.01$; Supplementary Fig. 12a) and pSTAT3 (Fig. 6a; $p \leq 0.05$) in the mesenchymal-like, vimentin-positive PDAC biopsies excised from patients with shorter median survival. The PDAC tissue with confirmed SMAD4 mutations also had elevated levels of epithelial pSTAT3 ($p \leq 0.001$), tenascin C ($p \leq 0.001$), fibronectin ($p \leq 0.01$) and collagen 12 ($p \leq 0.05$) (Fig. 6b). The epithelium in the PDAC tumors with mutated SMAD4 was more mechanically activated

as evidenced by a significant increase in nuclear YAP1 ($p \leq 0.01$). Moreover, the samples with SMAD4 mutations had significantly higher nuclear SOX2 ($p \leq 0.01$) and contained significantly more vimentin ($p \leq 0.001$) which is consistent with a quasi-mesenchymal phenotype that typically has a more aggressive disease pathology (Supplementary Fig. 12b).

Discussion

Using clinical specimens and experimental mouse models, we identified a unique, highly rigid, matricellular-stromal phenotype linked specifically to a PDAC genotype that results in reduced epithelial TGF-β signaling and elevated tumor cell contractility. Our data suggest that the genetically-induced tumor cell tension differentially "tunes" the composition and mechanics of the periductal stroma in PDACs, regardless of the bulk stromal phenotype, to promote tumor progression and aggression by engaging mechanosignaling pathways linked to integrins and YAP. The findings are consistent with the mathematical predictions identifying two distinct stromal phenotypes termed "normal" versus "activated" in PDAC subtypes of increasing aggression[24]. Our findings provide the first direct evidence that tumor genotype, per se, can calibrate tumor cell contractility to modulate the fibrotic phenotype of the tissue and modify the pathology of the cancer. Our data further suggest that bulk collagen content is a poor surrogate for the multi-faceted contributions of PDAC fibrosis to cancer aggression, and advocate imaging approaches to visualize differential distribution of the stroma such as MR imaging and elastography[52].

PDAC-associated fibrosis has been viewed as a constraint that directly compromises lymphatic drainage and impedes neovascularization, and indirectly increases interstitial fluid pressure to disrupt blood vessel integrity and induce hypoxia[1]. This physical barrier compromises drug delivery, reduces immune cell accessibility and promotes disease aggression and therapy resistance, underscoring the critical importance of tissue mechanics to tumor biology[12_4,53]. Importantly, our data show that the fibrosis is not merely a passive physical restraint. Rather, the elevated tissue mechanics directly activate key pathways such as integrin-dependent signaling and YAP to promote tumor progression and aggression[10_12]. To this end, our clinical findings revealed that poorly differentiated PDACs and the PDACs with impaired TGF-β signaling were the most mechanically-activated and expressed elevated YAP and SOX2, which are transcriptional regulators that have been implicated in tumor aggression and epithelial-to-mesenchymal transition[54_57]. Indeed, these same YAP- and SOX2-expressing tumors expressed markers of a mesenchymal-like phenotype including vimentin, fibronectin and tenascin C (Fig. 6b)[58_60]. Our findings thus imply that the more aggressive phenotype of PDACs with a quasi-mesenchymal phenotype may be linked to their altered mechano-behavior. Moreover, given that YAP signaling can drive Kras-independent PDAC growth and survival, our observations indicate that fibrotic PDAC tumors may naturally evolve towards Kras independence and that this phenotype will be potentiated by specific tumor genotypes that increase tissue fibrosis including loss of TGF-β signaling. Our data thereby present one plausible reason why there has been such a mixed response of PDAC cancer patients to anti-stromal therapies, and suggest that FAK and JAK inhibitors, which target both stroma and epithelial-driven fibrosis, and both of which reduced YAP and tenascin induction in our studies, may comprise more efficacious therapeutic options.

Experimental procedures

Human samples

Formalin-fixed, paraffin-embedded human PDAC tissue sections, lacking any patient-identifying information, were commercially purchased from US Biomax (PA961a) or obtained from cohort of patients based on long and short survival. For non-commercial human samples, the study was approved by Regional Scientific Ethics Committee of the Capital Region of Denmark (protocol H-KA-20060181) in Region Hovedstaden, Denmark. The use of control materials was approved by the Ethical Committees in Bergen, Norway and in Heidelberg, Germany[32]. Informed consent was obtained from human subjects. Snap-frozen human PDAC tissues were collected from autopsy participants with stage IV disease in association with the Gastrointestinal Cancer Rapid Medical Donation Program (GICRMDP) and the study was approved by the Johns Hopkins Institutional Review Board (protocol 36610,[36]).

Mice studies

All mice were maintained in accordance with University of California Institutional Animal Care and Use Committee guidelines under protocol number AN105326-01D. Transgenic mouse strains, $Kras^{LSL\text{-}G12D/+}$;Ptf1a-Cre (KC;[37]), $Kras^{LSL\text{-}G12D/+}$;$Tgfbr2^{flox/wt\ or\ flox/flox}$;Ptf1a-Cre (KTC;[22]); $Kras^{LSL\text{-}G12D/+}$;$Tp53^{R172H/+}$; Pdx1-Cre (KPC;[38]) LSL-β1V737N[48], $Stat3^{flox/flox}$ [51] and constitutively active Stat3C[50] were described previously. Mice were interbred and maintained in mixed background. Aged matched littermates not expressing Cre as well as Ptf1a-Cre and Pdx1-Cre mice were used as controls with mixed sexes were used for all experiments with the exception of xenografts studies which only included female mice.

For FAK inhibition studies, Ptf1a-Cre/β1-V737N mice were treated with FAK inhibitor PND-1186 at 0.5 mg/ml in 5% sucrose in the drinking water, control mice were provided 5% sucrose as drinking water ($n = 5$ per group). Treatment started at 3 weeks of age. At this time point, mice exhibit pancreatitis and fibrosis at 3 weeks of age and mice were killed after 3 weeks due to animal protocol guidelines. For JAK inhibition, KTC mice were treated with JAK inhibitor Ruxolitinib twice daily by oral gavage at 60 mg/kg body weight in 0.5% methylcellulose in water. Control mice were provided 0.5% methylcellulose in water ($n = 5$ per group). Treatment started at 3 weeks and mice were killed after 3 weeks. Mixed sexes were used for all experiments with the exception of xenograft studies which only included female mice.

For orthotopic xenografts, 5×10^5 firefly luciferase-mApple expressing cells in Matrigel (BD Biosciences) were injected into the pancreas of 8-week old nude mice (Simonsen laboratory) (n = 5 per group) and tumor growth was monitored by weekly bioluminescent imaging. Mice were sacrificed at 2 weeks following the cell injection due to animal protocol. Female mice were used in the xenografts studies.

For bioluminescent imaging animals were injected intraperitoneally with 3 mg of D-Luciferin and imaged using IVIS spectrum imaging system. The living imaging 4.3 software was used for analysis of the images post acquisition.

For all animal studies, animals were randomly distributed among the different conditions by the investigator since the animals did not exhibit any size or appearance differences at the onset of the experiments. No animals were excluded, and the investigator was not blinded during the experiment.

Histology

Paraffin-embedded or Fresh frozen pancreatic tissues were analyzed by H&E, picrosirius red, masson's trichrome or alcian blue according to the manufacturer's instructions. For mouse and clinical studies, staining intensity of tissue sections was scored blinded pathologist.

LC-MS/MS and LC-SRM Proteomic analysis

Proteomic analysis was performed in triplicate on 5 milligrams of fresh frozen KC, KPC, and KTC pancreatic tissues as previously described[61]. Briefly, tissues were milled in liquid N2 followed by sequential extraction of cellular proteins, soluble ECM proteins, and insoluble ECM proteins. Tryptic digests of all fractions were analyzed by liquid chromatography-select reaction monitoring LC-SRM mass spectrometry. Stable Isotope Labeled (SIL) peptides were used for absolute quantification of ECM proteins by LC-SRM.

Atomic force microscopy measurements

Atomic force microscopy and analysis were performed as previously described[62]. Frozen tissue blocks were cut into 20 μm thick sections. Prior to the atomic force microscopy (AFM) measurement, each section was immersed in PBS and thawed at room temperature. The samples were maintained in proteinase inhibitor in PBS (protease inhibitor cocktail, Roche 14 Diagnostics, 11836170001) supplemented with Propidium Iodide (SIGMA P4170, 20 μg/ml) during the AFM session. Five samples for each group were used for AFM quantification of Young's elastic modulus of the cancer-associated stroma. AFM indentations were performed using an MFP3D-BIO inverted optical AFM (Asylum Research) mounted on a Nikon TE2000-U inverted fluorescent microscope, as previously described (Lopez et al., 2011). Briefly, we used silicon nitride cantilevers with spring constant of 0.06 N/m with borosilicate glass spherical tip with 5 μm in diameter (Novascan Tech). The cantilever was calibrated using the thermal oscillation method prior to each experiment. Samples were indented at a 20 μm/s loading rate, with a maximum force of 2 nN. Five AFM force maps were typically obtained on each sample, each map as a 10×10 μm raster series of indentations utilizing the FMAP function of the IGOR PRO build supplied by Asylum Research. The Hertz model was used to determine the elastic properties of the tissue (E1). Tissue samples were assumed to be incompressible and a Poisson's ratio of 0.5 was used in the calculation of the Young's elastic modulus.

Two-photon second harmonics microscopy and image analysis

Two-photon imaging of pancreatic tissues and collagen gels was performed and quantified as previously described[63]. For two-photon imaging, we used custom resonant-scanning instruments based on published designs containing a 5-PMT array (Hamamatsu, C7950) operating at video rate (11). The setup was used with 2 channel simultaneous video rate

acquisition via 2 PMT detectors and an excitation laser (2W MaiTai Ti-Sapphire laser, 710–920 nm excitation range). Second harmonics imaging was carried out on a Prairie Technology Ultima System attached to an Olympus BX-51 fixed stage microscope equipped with a ×25 (NA 1.05) water immersion objective. Unfixed, hydrated samples were exposed to polarized laser light at a wavelength of 830 nm and emitted light was separated with a filter set (short pass filter, 720 nm; dichroic mirror, 495 nm; band pass filter, 475/40 nm). Images of×and y planes of 284 by 284 μm at a resolution of 0.656 μm/pixel were captured using Micro-Manager Open Source Microscopy Software (Micro-Manager). Quantification of collagen fibers was achieved by setting a minimal threshold in the second harmonic signal. The threshold was maintained for all images across all conditions. The area of regions that was covered by the minimal threshold was calculated and 3 images per sample were averaged together (Image J, Image Processing and Analysis in Java). Collagen fiber diameters data were visualized and analyzed using Imaris (Bitplane AG) and MATLAB (MathWorks).

Cell culture and establishment of primary pancreatic cell lines

Establishment of primary pancreatic tumor cells was performed as described previously[64]. Cells were maintained in RPMI-1640 medium containing 10% FBS (Clontech). All experiments were performed within eight passages to avoid possible gross genomic changes during long-term in vitro culture. Cells were verified by epithelial morphology in two dimensions (2D), expression of the epithelial marker cytokeratin 19 and the ability to form tumors *in vivo*. Cells were tested for mycoplasma contamination using commercially available kit (PCR-Mycoplasma Test Kit I/C (Promokine PK-CA91-1024) according to manufacturer's manual at the onset of the work (tested negative) and have never exhibited contamination symptoms after the test. Derivative cells were transduced in vitro with a lentiviral vector-encoding firefly Luciferase and mApple fluorescent protein for combined bioluminescent imaging and flow sorting. To ensure that all cell lines expressed similar levels of luciferase, mApple expressing cells were flow sorted prior to injection into animals.

Soft agar assay

Anchorage-independent growth was assessed using a soft agar assay ([65]). In brief, 25,000 cells in 1.5 ml 0.35% agarose containing 1× growth media were overlaid with 1.5 ml 0.5% agarose containing 1× growth media, and colonies larger than 30 μm in diameter were scored positive after 14 days.

Lentivirus-mediated shRNA knockdown

Lentiviral shRNA targeting ROCK1, ROCK2 and FAK and nontargeting shRNA control were cloned in the pLKO vector. The clone IDs for shRNA are as follows: sh-ROCK1 (TRCN0000022903), sh-ROCK2 (TRCN0000022922), sh-FAK (TRCN0000023485) and eEGFP as a non specific control cloned into the lentiviral pLKO.1 puro vector (Sigma-Aldrich).

Preparation of luciferase-mApple Virus-Infected Cells

Lentivirus infection was performed with pLKO EEF1α mApple luc2 lentiviral vector for combined flow sorting and *in vivo* imaging. This was constructed from the pLKO.1 puro vector by inserting an in-frame fusion of mApple with the human codon optimized firefly luciferase gene from pGL4.10[luc2] (Promega) and placing this under control of the human EEF1α promoter. This cassette, followed by a WPRE element was inserted in place of the U6 cppt mPGK puro elements in pLKO.1 puro (from claI to kpnI sites).

Quantitative real-time PCR

RNA was extracted using trizol/chloroform isolation followed by Ambion mirVana kit (AM1560). Total RNA was reverse-transcribed using random primers (Amersham Biosciences), and β-actin primers were used to control for cDNA concentration in a separate PCR reactions for each sample. LightCycler Fast Start DNA Master SYBR Green Mix (Roche) was added to each PCR reaction along with cDNA and 1 pmol primer in a total volume of 10 μl. qPCR was performed on a eppendorf realplex2 mastercycler using the real-time primers provided, according to instructions. Ct values were converted to fold expression changes ($2^{-\Delta\Delta Ct}$ values) following normalization to β-actin. Primer sequences are listed below.

Gene	Sequence
CTGF	F 5'-GTGAGTCCTTCCAAAGCAGC-3'
	R 5'-TAGTTGGGTCTGGGCCAAAT-3'
β-actin	F 5'-GTGGGCCGCCCTAGGCACCA-3'
	R 5'-CGGTTGGCCTTAGGGTTCAGGG-3'

Traction force microscopy

Traction of pancreatic cells was measured as previously described[18,66]. Images of cells on PA gels containing fluorescent beads were collected before and after trypsinization using a Nikon Inverted Eclipse TE300 microscope and a Photometric Cool Snap HQ camera (Roper Scientific). TFMs were calculated based on differences in bead displacement induced by substrate deformation and relaxation using a software analysis program.

Three dimensional collagen contraction assay

Collagen contraction assay was performed as previously described[42] Briefly, collagen I solution was prepared by neutralizing acid-solubilized rat tail collagen I (BD Bioscience) with 1 N NaOH and a DMEM buffer, 300 ul/well in 24 well plate and polymerized at 37 C. Cells were seeded on top of collagen and allowed to adhere overnight. Collagen gel area was quantified using NIH ImageJ analysis software.

Polyacrylamide substrates

Basement membrane–conjugated polyacrylamide hydrogels were prepared as previously described (Lakins, *Methods Mol. Biol.* **916**, 317–350 (2012) with one modification: *n*-succinimidyl acrylamidohexanoic acid crosslinker was conjugated to polyacrylamide substrates using 0.01% bisacrylamide, 0.025% Irgacure 2959 0.002% Di(trimethylolpropane) tetracrylate (Sigma) and 0.01% *n*-succinimidyl acrylamidohexanoic acid.

Cytokine antibody array

Proteins from the pancreatic cells or tissues were screened by using the Mouse Cytokine Antibody Array A (R&D ARY006) according to the manufacturer's instructions. In brief, conditioned media or protein lysate were collected and subjected to the antibody array incubation. The amount of conditioned media used was normalized by the cell number. The membranes were washed and incubated with primary biotin-conjugated antibody and then incubated with horseradish peroxidase–conjugated streptavidin, and the protein spots were detected using the ECL Western blotting detection reagents (GE Healthcare) according to the manufacturer's instructions. The spot density was quantified and compared between different conditions.

Tissue processing and Immunostaining

Fresh tumors were harvested, embedded in O.C.T. medium (TissueTek) prior to freezing in liquid nitrogen. Frozen sections 5 μm thick were fixed in PFA for 15 min. Paraffin embedded harvested tumors were formalin fixed prior to paraffin embedding. Sections 5 μm thick were deparaffinized, rehydrated and boiled for 1 hour in 10mM citrate buffer at pH 6.0. For all stains, the tissue sections were blocked with 5% normal goat serum/0.3% Triton™ X-100 in PBS for 60 minutes at room temperature. Sections were then incubated with primary antibodies overnight at 4C followed by incubation with fluorochrome conjugated secondary antibodies for 1 hour at room temperature. 1% BSA/0.3% Triton™ X-100 in PBS was used to dilute primary and secondary antibodies. DAPI was used to stain cell nuclei. All stainings were quantified using NIH ImageJ analysis software with the same threshold for each stain; positivity was analyzed in five visual fields for each sample and results were expressed as percentage staining per visual field.

Antibodies and reagents

Antibodies were as follows: a-SMA (Sigma-Aldrich C6198, 1:1000), GLi-1 (Thermo Scientific PA5-32206, 1:500), Tenascin C (Abcam AB108930, 1:500), Fibronectin (Abcam AB2413, 1:500), Collagen 12A1 (Santa Cruz Biotechnology E-15 sc-68449, 1:200), Sox2 (Abcam ab97959, 1:500), Vimentin (Cell Signaling 5741S, 1:200), FAP (Abcam AB53066, 1:500), Collagen III (Abcam AB7778, 1:500), YAP (Cell signaling 4912, 1:200), β1integrin (EMD Millipore MABT409, 1:500), pY397-FAK (Invitrogen 44625, 1:200), total FAK (BD Biosciences 610088, 1:1,000), ROCK1 (Cell Signaling C8F7, 1:1,000), ROCK2 (Cell Signaling D1B1, 1:1,000), p-MLC2 (Cell Signaling 3671, 1:200), p-MyPT1 (Millipore ABS45, 1:200), p-Stat3 (Cell Signaling 9145, 1:200), p-SMAD2/3 (Cell Signaling 8828, 1:200), total Stat3 (Cell Signaling 9132, 1:1,000), GAPDH (Cell Signaling 2118, 1:5,000),

CD45 (BD Biosciences 550539, 1:200), CD68 (Thermo Scientific Ab-3, 1:200), Alexa Fluor-conjugated goat secondary anti–mouse IgG and anti–rabbit IgG antibodies (Invitrogen A11012, 1:1,000 and A11005, 1:1,000) and HRP-conjugated rabbit secondary antibody (GE health care life sciences NA934VS, 1:5,000).

Immunoblotting

Iimmunoblotting analysis were performed as previously described[67]. In brief, equal amounts of cell protein lysate (Laemmli) were separated on reducing SDS-PAGE gels, transferred to nitrocellulose membrane, and probed with primary antibody. Bands were visualized and quantified using a PXI 6 Touch (Syngene), in conjunction with HRP-conjugated secondary antibodies and ECL (Amersham Pharmacia).

Flow sorting

Weighed tumors were minced and allowed to digest in a mixture of 1mg/ml of collagenase P (Roche 11213857001), 0.1 mg/ml Collagenase I (Sigma, C0130), 0.1 mg/ml Dispase II (Roche, 04942078001) and DNase (5MU/ml, Calbiochem, 260913) in DMEM media at 37°C for 30 min. The tissue lysate was filtered through a 40 μm mesh prior to immunostaining. The resulting single-cell suspension was stained with fixable viability dye eFluor 780, anti-CD45-APC-Cy7 (103115, 1:200), anti-CD11b-FITC (101205, 1:100) and anti-Ly6/C-PE (128007, 1:100) (all from BioLegend). The percentage of positive cells were analyzed by FlowJo and gated on CD45 positivity. Unstained, live/dead only, and single stain served as control. Doublets were gated out using forward-scatter width/height and side-scatter width/height event characteristics.

Bioinformatics

Patient expression data was pulled from publicly available dataset GSE21501 obtained from NCBI GEO. Following baseline normalization, expression values for Col1a2, Col2a1, and Col4a1 were used to create a median centroid value representing an average collagen expression score for each patient. These values were then divided into high and low expression based on median centroid value for the patient set and graphed as survival of each group over time. Kaplan–Meier survival curves were analyzed by Cox–Mantel Log-rank analysis.

Statistics

All quantitative results were assessed by unpaired Student's t-test after confirming that the data met appropriate assumptions (normality, homogenous variance, and independent sampling), non-parametric Wilcox/Mann Whitney exact test (using the normal approximation for the U score), or the Kolmogorov-Smirnov distribution test, all two-tailed. For all *in vitro* experiments, 3 technical replicates were analyzed for each experiment and results are presented as the mean +/− SEM of 3 biological replicates. For all in vivo experiments, 5 biological replicates were analyzed for each condition and results are presented as the mean +/− SEM. Subsequent statistical analysis was performed with either unpaired two-sided student t-tests, one-way ANOVA with Tukey's method for multiple comparisons. For survival analysis, the log-rank (Mantel-Cox) test was used. Prism software

was used to conduct the statistical analysis of all data. P-values of less than 0.05 were considered to be significant. *p<0.05; **p<0.01, ***p<0.001, ****p<0.0001, “ns” denotes not significant for all experiments. Sample size estimation was initially performed using the Mann-Whitney test (Lab. Animal Sci. 41:6-16, 1991) as a guide and taking into consideration previous experience with assay sensitivity, tissue collection and the different animal strains utilized. For the listed sample size per group at each time point, the numbers provide a minimum of 85% power to detect an effect size of 2.5 (tumor size, stiffness, gene expression, protein expression) with two-sided type I error = 5% ($p \leq 0.05$). The effect size is defined (where applicable). For animal studies, animals were randomly distributed among the different conditions by the investigator since the animals did not exhibit any size or appearance differences at the onset of the experiments. No animals were excluded, and the investigator was not blinded during the experiment. For mouse and clinical studies, staining intensity of tissue sections was scored blinded.

Supplementary Material

Refer to Web version on PubMed Central for supplementary material.

Acknowledgments

We thank Dr. M. Dembo for the LIBTRC 2.0 traction force software. Animal handling was supported by L. Korets. This work was supported by US National Institutes of Health NCI grants U01 CA151925-01 (V.M.W., H.L.M. and R.K.), R33 CA183685-01 (V.M.W., K.H.), R01 CA138818-01A1 (V.M.W.), U54CA143836-01 (V.M.W.), CA102310 (D.D.S.), R01CA178015-02 (E.A.C.), R01 CA172045 (M.H.), T32CA108462 (M.W.P.), F31CA180422 (Y.A.M.), the Pancreatic Cancer Action Network- AACR Innovative Grant 30-60-25-WEAV (V.M.W.), NSF GRFP 1144247 (Y.A.M.) and NIH TL1 TR001081 (A.S.B.).

References

1. Chauhan VP, et al. Angiotensin inhibition enhances drug delivery and potentiates chemotherapy by decompressing tumour blood vessels. Nat. Commun. 2013; 4:2516. [PubMed: 24084631]
2. Swartz MA, Lund AW. Lymphatic and interstitial flow in the tumour microenvironment: linking mechanobiology with immunity. Nature Reviews Cancer. 2012; 12:210–219. [PubMed: 22362216]
3. Yu M, Tannock IF. Targeting Tumor Architecture to Favor Drug Penetration: A New Weapon to Combat Chemoresistance in Pancreatic Cancer? Cancer Cell. 2012; 21:327–329. [PubMed: 22439929]
4. Provenzano PP, Hingorani SR. Hyaluronan, fluid pressure, and stromal resistance in pancreas cancer. Br. J. Cancer. 2013; 108:1–8. [PubMed: 23299539]
5. Olive KP, et al. Inhibition of Hedgehog signaling enhances delivery of chemotherapy in a mouse model of pancreatic cancer. Science. 2009; 324:1457–1461. [PubMed: 19460966]
6. Provenzano PP, et al. Enzymatic targeting of the stroma ablates physical barriers to treatment of pancreatic ductal adenocarcinoma. Cancer Cell. 2012; 21:418–429. [PubMed: 22439937]
7. Rosow DE, et al. Sonic Hedgehog in pancreatic cancer: from bench to bedside, then back to the bench. Surgery. 2012; 152:S19–S32. [PubMed: 22770959]
8. Ozdemir BC, et al. Depletion of carcinoma-associated fibroblasts and fibrosis induces immunosuppression and accelerates pancreas cancer with reduced survival. Cancer Cell. 2014; 25:719–734. [PubMed: 24856586]
9. Rhim AD, et al. Stromal elements act to restrain, rather than support, pancreatic ductal adenocarcinoma. Cancer Cell. 2014; 25:735–747. [PubMed: 24856585]
10. Jain RK, Martin JD, Stylianopoulos T. The role of mechanical forces in tumor growth and therapy. Annu Rev Biomed Eng. 2014; 16:321–346. [PubMed: 25014786]

11. Neesse A, et al. Stromal biology and therapy in pancreatic cancer. Gut. 2011; 60:861–868. [PubMed: 20966025]
12. Stromnes IM, DelGiorno KE, Greenberg PD, Hingorani SR. Stromal re-engineering to treat pancreas cancer. Carcinogenesis. 2014; 35:1451–1460. [PubMed: 24908682]
13. Cheung KJ, Gabrielson E, Werb Z, Ewald AJ. Collective invasion in breast cancer requires a conserved basal epithelial program. Cell. 2013; 155:1639–1651. [PubMed: 24332913]
14. Hoadley KA, et al. Multiplatform Analysis of 12 Cancer Types Reveals Molecular Classification within and across Tissues of Origin. Cell. 2013
15. Collisson, Ea, et al. Comprehensive molecular profiling of lung adenocarcinoma. Nature. 2014; 511:543–550. [PubMed: 25079552]
16. Sugimoto H, Mundel TM, Kieran MW, Kalluri R. Identification of fibroblast heterogeneity in the tumor microenvironment. Cancer Biol. Ther. 2006; 5:1640–1646. [PubMed: 17106243]
17. Wang Y, You M. Alternative splicing of the K-ras gene in mouse tissues and cell lines. Exp Lung Res. 2001; 27:255–267. [PubMed: 11293328]
18. Paszek MJ, et al. Tensional homeostasis and the malignant phenotype. Cancer Cell. 2005; 8:241–254. [PubMed: 16169468]
19. Samuel MS, et al. Actomyosin-mediated cellular tension drives increased tissue stiffness and β-catenin activation to induce epidermal hyperplasia and tumor growth. Cancer Cell. 2011; 19:776–791. [PubMed: 21665151]
20. Iacobuzio-Donahue CA, et al. DPC4 gene status of the primary carcinoma correlates with patterns of failure in patients with pancreatic cancer. J Clin Oncol. 2009; 27:1806–1813. [PubMed: 19273710]
21. Whittle MC, et al. RUNX3 Controls a Metastatic Switch in Pancreatic Ductal Adenocarcinoma. Cell. 2015; 161:1–16.
22. Ijichi H, et al. Aggressive pancreatic ductal adenocarcinoma in mice caused by pancreas-specific blockade of transforming growth factor-β signaling in cooperation with active Kras expression. Genes Dev. 2006; 20:3147–3160. [PubMed: 17114585]
23. Collisson, Ea, et al. Subtypes of pancreatic ductal adenocarcinoma and their differing responses to therapy. Nat. Med. 2011; 17:500–503. [PubMed: 21460848]
24. Moffitt RA, et al. Virtual microdissection identifies distinct tumor- and stroma-specific subtypes of pancreatic ductal adenocarcinoma. Nat. Genet. 2015; 47:1168–1178. [PubMed: 26343385]
25. Kabashima A, et al. Side population of pancreatic cancer cells predominates in TGF-beta-mediated epithelial to mesenchymal transition and invasion. Int. J. Cancer. 2009; 124:2771–2779. [PubMed: 19296540]
26. Dangi-Garimella S, et al. Three-dimensional collagen I promotes gemcitabine resistance in pancreatic cancer through MT1-MMP-mediated expression of HMGA2. Cancer Res. 2011; 71:1019–1028. [PubMed: 21148071]
27. Erkan M, et al. The Activated Stroma Index Is a Novel and Independent Prognostic Marker in Pancreatic Ductal Adenocarcinoma. Clin. Gastroenterol. Hepatol. 2008; 6:1155–1161. [PubMed: 18639493]
28. Sinn M, et al. α-Smooth muscle actin expression and desmoplastic stromal reaction in pancreatic cancer: results from the CONKO-001 study. Br. J. Cancer. 2014; 111:1917–1923. [PubMed: 25314063]
29. Bever KM, et al. The prognostic value of stroma in pancreatic cancer in patients receiving adjuvant therapy. Hpb. 2014 n/a–n/a.
30. Wang WQ, et al. Intratumoral α-SMA Enhances the Prognostic Potency of CD34 Associated with Maintenance of Microvessel Integrity in Hepatocellular Carcinoma and Pancreatic Cancer. PLoS One. 2013; 8
31. Rath N, Olson MF. Rho-associated kinases in tumorigenesis: re-considering ROCK inhibition for cancer therapy. EMBO Rep. 2012; 13:900–908. [PubMed: 22964758]
32. Schultz, Na, et al. MicroRNA expression profiles associated with pancreatic adenocarcinoma and ampullary adenocarcinoma. Mod. Pathol. 2012:1609–1622. [PubMed: 22878649]

33. Pérez-Mancera PA, Guerra C, Barbacid M, Tuveson DA. What we have learned about pancreatic cancer from mouse models. Gastroenterology. 2012; 142:1079–1092. [PubMed: 22406637]
34. Macias MJ, Martin-Malpartida P, Massagué J. Structural determinants of Smad function in TGF-β signaling. Trends Biochem. Sci. 2015; 40:296–308. [PubMed: 25935112]
35. Shi Y, Massagué J. Mechanisms of TGF-beta signaling from cell membrane to the nucleus. Cell. 2003; 113:685–700. [PubMed: 12809600]
36. Yachida S, et al. Clinical significance of the genetic landscape of pancreatic cancer and implications for identification of potential long-term survivors. Clin. Cancer Res. 2012; 18:6339–6347. [PubMed: 22991414]
37. Hingorani SR, et al. Preinvasive and invasive ductal pancreatic cancer and its early detection in the mouse. Cancer Cell. 2003; 4:437–450. [PubMed: 14706336]
38. Hingorani SR, et al. Trp53R172H and KrasG12D cooperate to promote chromosomal instability and widely metastatic pancreatic ductal adenocarcinoma in mice. Cancer Cell. 2005; 7:469–483. [PubMed: 15894267]
39. Dupont S, et al. Role of YAP/TAZ in mechanotransduction. Nature. 2011; 474:179–183. [PubMed: 21654799]
40. Blackford A, et al. SMAD4 gene mutations are associated with poor prognosis in pancreatic cancer. Clin. Cancer Res. 2009; 15:4674–4679. [PubMed: 19584151]
41. Iacobuzio-Donahue, Ca, et al. DPC4 gene status of the primary carcinoma correlates with patterns of failure in patients with pancreatic cancer. J. Clin. Oncol. 2009; 27:1806–1813. [PubMed: 19273710]
42. Sanz-Moreno V, et al. ROCK and JAK1 Signaling Cooperate to Control Actomyosin Contractility in Tumor Cells and Stroma. Cancer Cell. 2011; 20:229–245. [PubMed: 21840487]
43. Fukuda A, et al. Stat3 and MMP7 Contribute to Pancreatic Ductal Adenocarcinoma Initiation and Progression. Cancer Cell. 2011; 19:441–455. [PubMed: 21481787]
44. Lesina M, et al. Stat3/Socs3 Activation by IL-6 Transsignaling Promotes Progression of Pancreatic Intraepithelial Neoplasia and Development of Pancreatic Cancer. Cancer Cell. 2011; 19:456–469. [PubMed: 21481788]
45. Nagathihalli NS, et al. STAT3 Mediated Remodeling of the Tumor Microenvironment Results in Enhanced Tumor Drug Delivery in a Mouse Model of Pancreatic Cancer. Gastroenterology. 2015:1–12.
46. Ijichi H, et al. Inhibiting Cxcr2 disrupts tumor-stromal interactions and improves survival in a mouse model of pancreatic ductal adenocarcinoma. J. Clin. Invest. 2011; 121:4106–4117. [PubMed: 21926469]
47. Schrader J, et al. Matrix stiffness modulates proliferation, chemotherapeutic response, and dormancy in hepatocellular carcinoma cells. Hepatology. 2011; 53:1192–1205. [PubMed: 21442631]
48. Mouw JK, et al. Tissue mechanics modulate microRNA-dependent PTEN expression to regulate malignant progression. Nat. Med. 2014; 20:360–367. [PubMed: 24633304]
49. Li R, et al. Activation of integrin alphaIIbbeta3 by modulation of transmembrane helix associations. Science. 2003; 300:795–798. [PubMed: 12730600]
50. Barbieri I, et al. Constitutively active Stat3 enhances neu-mediated migration and metastasis in mammary tumors via upregulation of Cten. Cancer Res. 2010; 70:2558–2567. [PubMed: 20215508]
51. Alonzi T, et al. Essential Role of STAT3 in the Control of the Acute-Phase Response as Revealed by Inducible Gene Activation in the Liver Essential Role of STAT3 in the Control of the Acute-Phase Response as Revealed by Inducible Gene Activation in the Liver. 2001; 21:1621–1632.
52. Luna A, Pahwa S, Bonini C. Multiparametric MR Imaging in Abdominal Malignancies. Magn. Reson. Imaging Clin. NA. 2016; 24:157–186.
53. Chauhan VP, et al. Compression of pancreatic tumor blood vessels by hyaluronan is caused by solid stress and not interstitial fluid pressure. Cancer Cell. 2014; 26:14–15. [PubMed: 25026209]
54. Herreros-Villanueva M, et al. SOX2 promotes dedifferentiation and imparts stem cell-like features to pancreatic cancer cells. Oncogenesis. 2013; 2:e61. [PubMed: 23917223]

55. Shao DD, et al. KRAS and YAP1 converge to regulate EMT and tumor survival. Cell. 2014; 158:171–184. [PubMed: 24954536]
56. Jiang J, et al. MiR-1181 inhibits stem cell-like phenotypes and suppresses SOX2 and STAT3 in human pancreatic cancer. Cancer Lett. 2015; 356:962–970. [PubMed: 25444909]
57. Yimlamai D, et al. Hippo pathway activity influences liver cell fate. Cell. 2014; 157:1324–1338. [PubMed: 24906150]
58. Kohler I, et al. Detailed analysis of epithelial-mesenchymal transition and tumor budding identifies predictors of long-term survival in pancreatic ductal adenocarcinoma. J. Gastroenterol. Hepatol. 2015; 30:78–84. [PubMed: 25827809]
59. Paron I, et al. Tenascin-c enhances pancreatic cancer cell growth and motility and affects cell adhesion through activation of the integrin pathway. PLoS One. 2011; 6
60. Esposito I, et al. Tenascin C and annexin II expression in the process of pancreatic carcinogenesis. J. Pathol. 2006; 208:673–685. [PubMed: 16450333]

References

61. Hill RC, Calle Ea, Dzieciatkowska M, Niklason LE, Hansen KC. Quantification of Extracellular Matrix Proteins from a Rat Lung Scaffold to Provide a Molecular Readout for Tissue Engineering. Mol. Cell. Proteomics. 2015; 14:961–973. [PubMed: 25660013]
62. Lopez JI, Kang I, You W-K, McDonald DM, Weaver VM. In situ force mapping of mammary gland transformation. Integr. Biol. (Camb). 2011; 3:910–921. [PubMed: 21842067]
63. Pickup MW, et al. Stromally derived lysyl oxidase promotes metastasis of transforming growth factor-β-deficient mouse mammary carcinomas. Cancer Res. 2013; 73:5336–5346. [PubMed: 23856251]
64. Aguirre AJ, et al. Activated Kras and Ink4a/Arf deficiency cooperate to produce metastatic pancreatic ductal adenocarcinoma. Genes Dev. 2003; 17:3112–3126. [PubMed: 14681207]
65. Damiano L, et al. Oncogenic targeting of BRM drives malignancy through C/EBPβ-dependent induction of α5 integrin. Oncogene. 2013; 33:2441–2453. [PubMed: 23770848]
66. Reinhart-King CA, Dembo M, Hammer DA. Endothelial cell traction forces on RGD-derivatized polyacrylamide substrata. Langmuir. 2003; 19:1573–1579.
67. Paszek MJ, et al. The cancer glycocalyx mechanically primes integrin-mediated growth and survival. Nature. 2014; 511:319–325. [PubMed: 25030168]

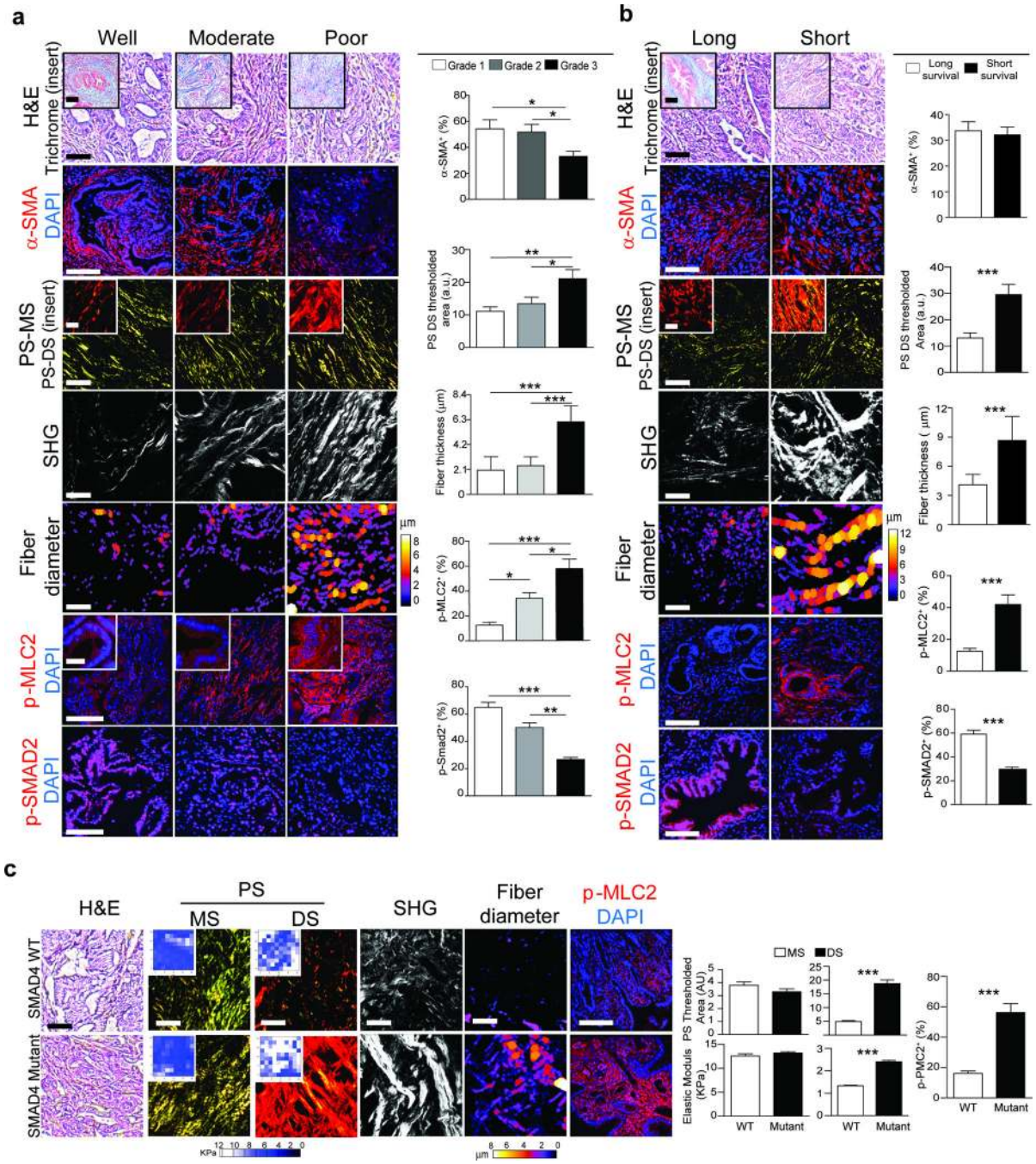

Figure 1. Tissue tension and collagen thickness linked to PDAC prognosis

(**a**) H&E and Trichrome (top insert) staining of PDAC tissue arrays for well ($n = 19$), moderately ($n = 23$) or poorly differentiated ($n = 26$) tumors; Scale bar, 100 μm (main) and 50 μm (insert). Immunofluorescence images and quantifications of α-SMA, p-MLC2, p-SMAD2 and DAPI; Scale bar, 75 μm (main) and 40 μm (insert). Polarized light images of picrosirius red (PR) within the main stroma (MS) (3rd) and periductal stroma (DS) (3rd insert); Scale bar, 50 μm (main) and 40 μm (insert). Second harmonic generation (SHG) of periductal collagen and diameter color-coded SHG; Scale bar, 75 μm. (**b**) H&E and

Trichrome (top insert) staining of tissue from PDAC patients with a median short survival of 11–289 days ($n = 29$) and median long survival of 1090–3298 days ($n = 28$); Scale bar, 100 μm. Immunofluorescence and quantification of tissue stained for α-SMA, p-MLC2, p-SMAD2 and DAPI; Scale bar, 75 μm. PR staining within the main stroma (MS) and periductal stroma (DS) (insert); Scale bar, 50μm. Periductal SHG and diameter color-coded SHG; Scale bar, 75 μm. (**c**) H&E staining of PDAC tissue from wild type SMAD4 ($n = 10$) and mutant SMAD4 ($n = 10$) patients. Scale bar, 100 μm. PR staining and quantification within the main stroma (MS) and periductal stroma (DS); Scale bar, 50 μm. Force maps and quantification of the main stroma (MS) (insert) and periductal stroma (DS) (insert). SHG of periductal collagen and diameter color-coded SHG; Scale bar, 75 μm. Immunofluorescence staining and quantification for p-MLC2 and DAPI; Scale bar, 75 μm. Results are presented as the mean +/− SEM. Subsequent statistical analysis was performed with either unpaired two-sided student t-tests, one-way ANOVA with Tukey's method for multiple comparisons. (*$P < 0.05$; **$P < 0.01$, ***$P < 0.001$, ****$P < 0.0001$, "ns" not significant).

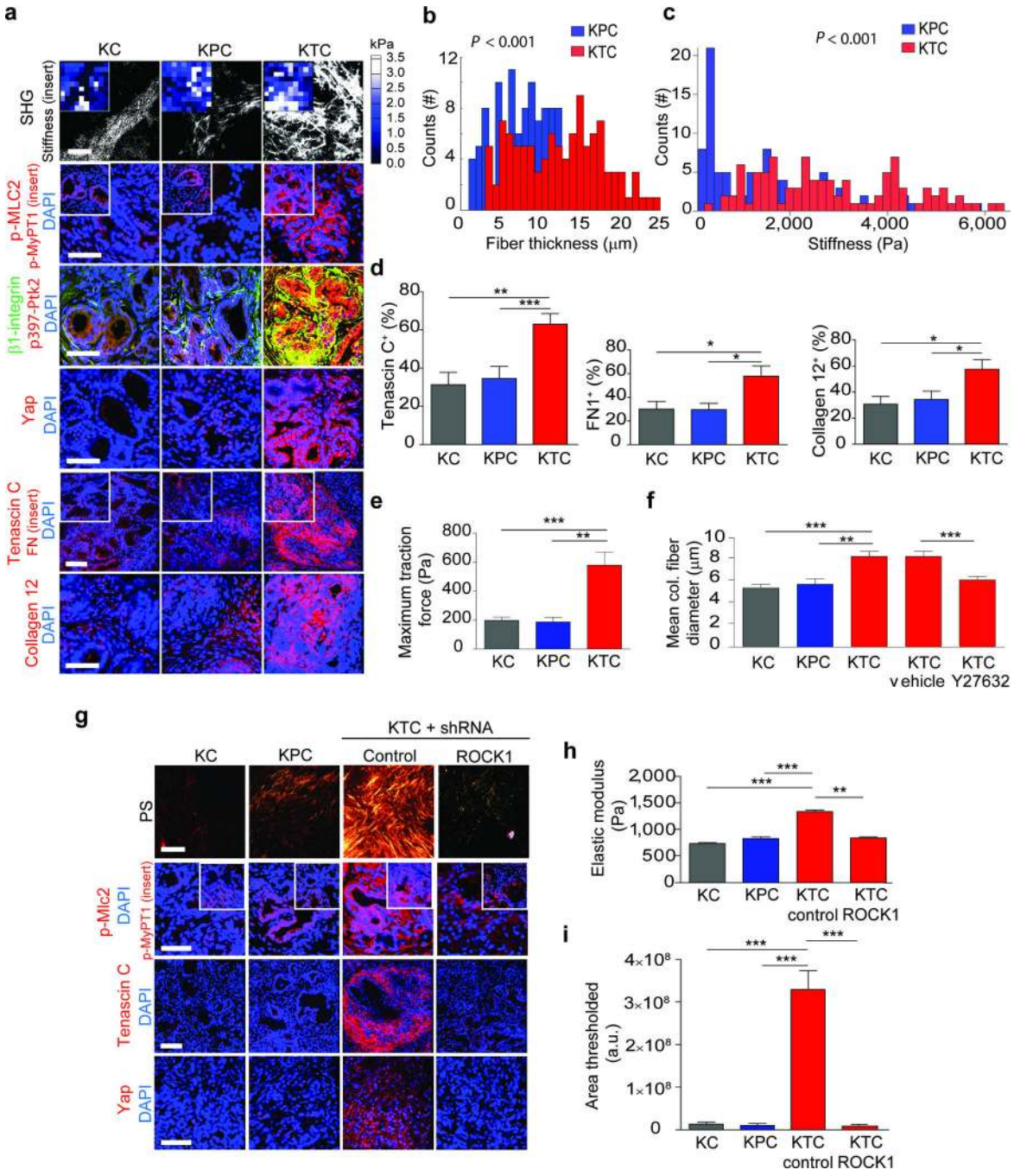

Figure 2. PDAC genotype tunes epithelial tension to regulate fibrosis

(**a**) SHG images from 20 week KC, KPC or KTC transgenic pancreatic tissues (top); Scale bar, 75 μm. Force maps from AFM PDAC ECM (top insert). Immunofluorescence images of p-Mlc2, p-MyPT1 (insert), β1-integrin and p-Ptk2, Yap1 and DAPI; Scale bar, 50 μm. Tenascin C, Fibronectin (insert), Collagen type XII alpha1 and DAPI; Scale bar, 75 μm. (**b**) Quantification of SHG fibril thickness and distribution around PDAC lesions. (**c**) Distribution of PDAC ECM stiffness measured by AFM. (**d**) Quantification of Tenascin C, Fibronectin and Collagen type XII alpha 1 images shown in (a). (**e**) Quantification of

traction force KC, KPC and KTC cells on 2300 Pa polyacrylamide gels. (**f**) Quantification of mean collagen fiber diameter in three-dimensional collagen gels with KC, KPC or KTC cells or with KTC cells treated with vehicle or ROCK inhibitor Y27632 at 24 hours. (**g**) PR staining of tissue excised from nude mice 3 weeks after injection with KC, KPC, or KTC cells expressing either a control shRNA or an shRNA to Rock1 (top); Scale bar, 75 μm. Immunofluorescence of p-Mlc2, p-MyPT1 (insert), Tenascin C, Yap1 and DAPI; Scale bar, 50 μm. (**h**) Quantification of stiffness of tissue in (e). (**i**) Quantification of total levels of fibrillar collagen. For *in vitro* bar graphs, 3 technical replicates were performed and results are the mean +/− SEM of 3 independent experiments. For *in vivo* experiments, $n = 5$ mice per group. Subsequent statistical analysis was performed with either unpaired two-sided student t-tests, one-way ANOVA with Tukey's method for multiple comparisons. For survival analysis, the log-rank (Mantel-Cox) test was used. (*$P < 0.05$; **$P < 0.01$, ***$P < 0.001$, ****$P < 0.0001$, "ns" not significant).

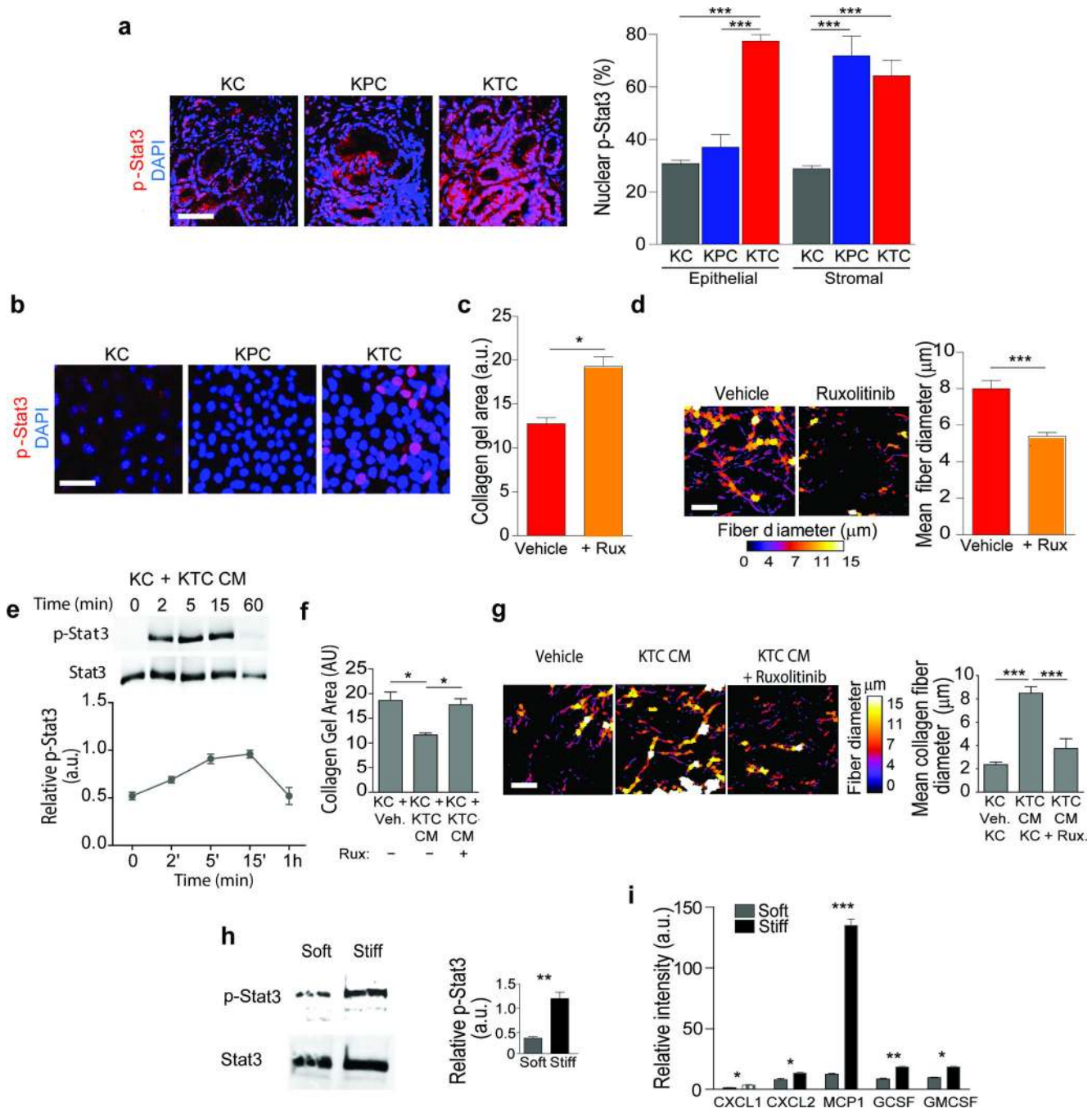

Figure 3. JAK-Stat3 signaling drives ECM remodeling and stiffening

(**a**) Immunofluorescence images and quantification of epithelial and stromal staining in 20 week old KC, KPC and KTC mice stained for pStat3 and DAPI; Scale bar, 50 μm. (**b**) Immunofluorescence images of KC, KPC and KTC tumor cells stained for p-Stat3 and DAPI; Scale bar, 25 μm. (**c**) Quantification of collagen contraction as measured by total collagen gel area in three dimensional collagen gels with KTC tumor cells for 24 hours either with vehicle or the Jak inhibitor Ruxolitinib. (**d**) Polarized light images and quantification of PR stained color-coded fibrillar collagen diameter on gels from (c); Scale

bar 75 μm. (**e**) Immunoblot and relative quantification of Stat3 activation (pStat3) in KC cells following exposure to KTC conditioned media (CM). (**f**) Quantification of collagen contraction measured by total collagen gel area of gels with KTC vehicle or Ruxolitinib CM treated KC tumor cells for 48 hours. (**g**) Polarized light images and quantification of PS, color-coded fibrillar collagen diameter; Scale bar 75 μm. (**h**) Immunoblot and relative quantification of total Stat3 and p-Stat3 levels in KC tumor cells cultured on soft or stiff polyacrylamide substrates. (**i**) Quantification of cytokine levels in the CM of KC cells cultured on soft or stiff polyacrylamide substrates. For *in vitro* quantification, results represent 3 technical replicates for and are the mean +/− SEM of 3 independent experiments. For *in vivo* experiments, $n = 5$ mice per group. Subsequent statistical analysis was performed with either unpaired two-sided student t-tests, one-way ANOVA with Tukey's method for multiple comparisons. For survival analysis, the log-rank (Mantel-Cox) test was used. (*$P <$ 0.05; **$P < 0.01$, ***$P < 0.001$, ****$P < 0.0001$, "ns" not significant).

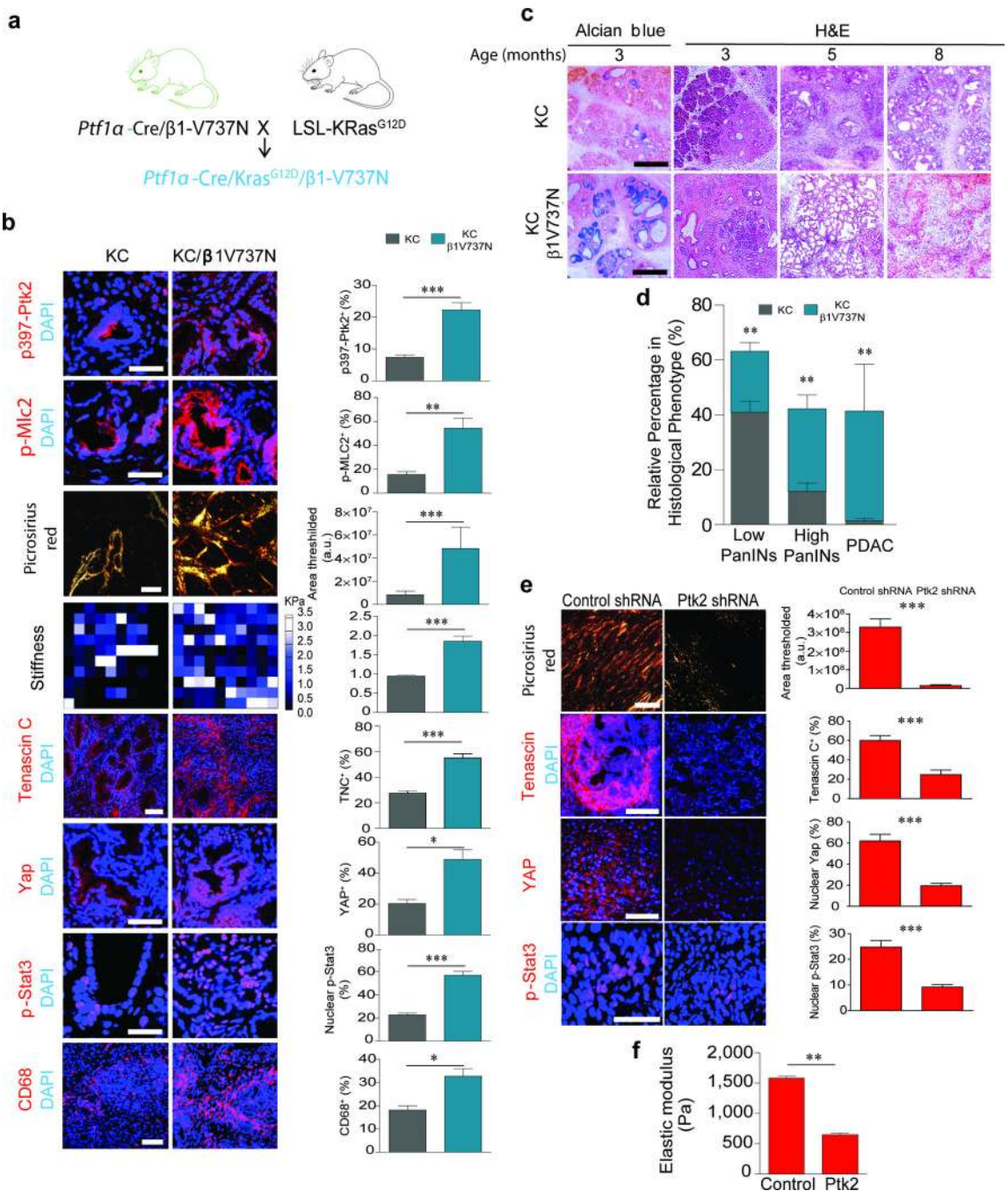

Figure 4. Tumor cell tension accelerates PDAC progression in mice

(**a**) Cartoon of mouse manipulations used to study the impact of increasing pancreatic epithelial cell mechanosignaling using β1-V737N on Kras-induced pancreatic malignancy. (**b**) Immunofluorescence images and quantification of pancreatic tissues from 3 month old KC and KC/β1-V737N mice stained for p397-Ptk2 and p-Mlc2, Tenascin C, Yap1, p-Stat3; Scale bar, 50 μm, CD68 and DAPI; Scale bar, 100 μm. Polarized light images of PS staining; Scale bar, 75 μm. Force maps of ECM stiffness. (**c**) Alcian blue H&E images of KC and KC/β1-V737N tissue; Scale bar, 100μm. (**d**) Quantification of histopathologic phenotypes

present in KC and KC+β1-V737N mice. (**e**) Polarized light images and quantification of PS staining of pancreatic tissues in nude mice injected with KTC tumor cells expressing either a control shRNA or a FAK shRNA; Scale bar, 75 μm. Immunofluorescence images and quantification of Tenascin C (scale bar 75 μm), Yap1 (75 μm), p-Stat3 (scale bar, 25 μm) and DAPI. (**f**) Quantification of average elastic modulus (Pa). For *in vivo* experiments, $n = 5$ mice per group. Subsequent statistical analysis was performed with unpaired two-sided student t-tests.. (*$P < 0.05$; **$P < 0.01$, ***$P < 0.001$, ****$P < 0.0001$, "ns" not significant).

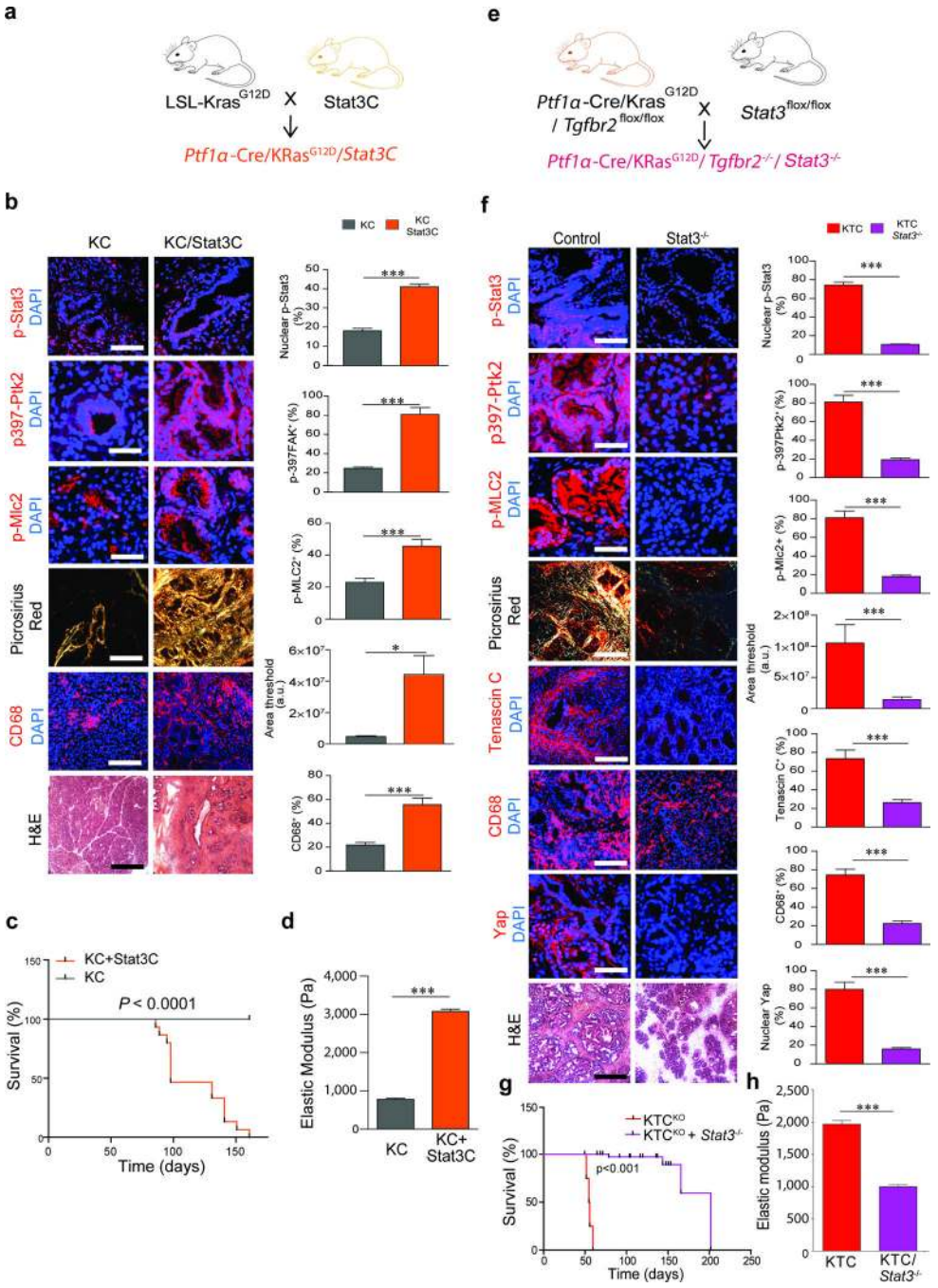

Figure 5. Stat3 induces fibrosis and accelerates PDAC

(**a**) Cartoon depicting the mouse crosses used for the activated Stat3C manipulations. (**b**) Immunofluorescence images and quantification of pancreatic tissues from 5 week old KC and KC/Stat3C mice stained for p-Stat3, scale bar, 75 μm, p397-Ptk2 and p-Myl2, scale bar, 50 μm, CD68, scale bar, 100 μm, and DAPI. Polarized light images and quantification of PS staining; Scale bar, 75 μm and H&E staining; Scale bar, 100 μm. (**c**) Kaplan-Meier graph showing survival of KC and KC/Stat3C mice. (**d**) Quantification of ECM stiffness in (b). (**e**) Cartoon depicting the mouse crosses used for the Stat3 knock studies. (**f**)

Immunofluorescence images and quantification of pancreatic tissues from 5 week old homozygous KTC (Control) and KTC+Stat3$^{-/-}$ mice (KTC Stat3$^{-/-}$) stained for p-Stat3, scale bar, 75 μm, p397-Ptk2 and p-Myl2, scale bar, 50 μm, Tenascin C, CD68, scale bar, 100 μm, Yap1 scale bar, 50 μm, and DAPI. Polarized light images and quantification of PS staining; Scale bar, 75 μm, and H&E staining. Scale bar, 100 μm. (**g**) Kaplan-Meier graph showing survival of KTC and KTC/Stat3 KO mice. (**h**) Quantification of ECM stiffness on tissue in (f). For *in vivo* experiments, $n = 5$ mice per group. Subsequent statistical analysis was performed with unpaired two-sided student t-tests. (*$P < 0.05$; **$P < 0.01$, ***$P < 0.001$, ****$P < 0.0001$, "ns" not significant).

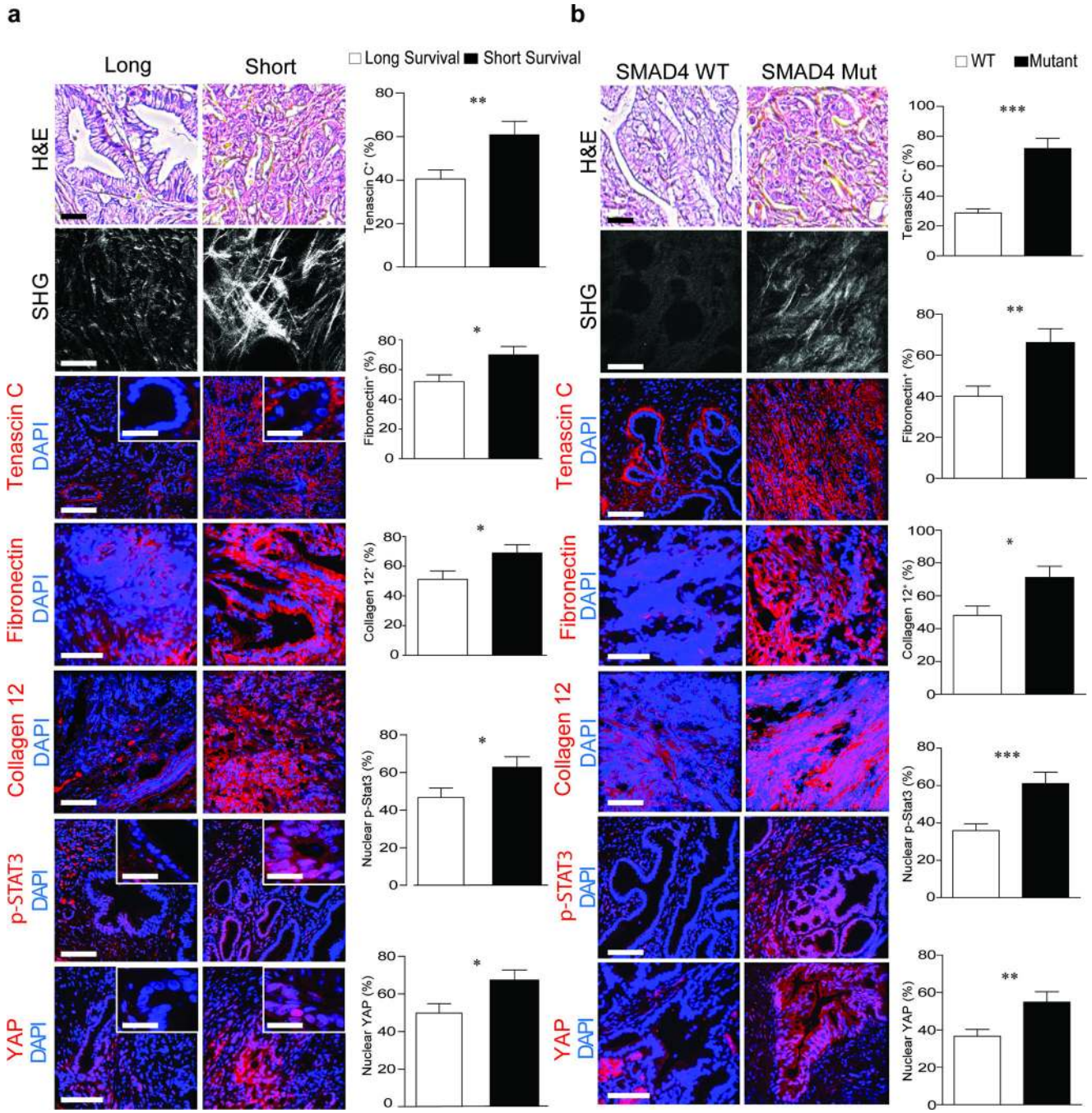

Figure 6. STAT3 enhances epithelial contractility to induce PDAC fibrosis and aggression

(**a**) H&E images of PDAC tumors from patients with a median short survival of 11–289 days ($n = 29$) and median long survival of 1090–3298 days ($n = 28$). Scale bar, 100 μm. SHG images and quantification of extracellular collagen architecture in the pancreatic tissue around the epithelial ductal region in tissue described above. Scale bar, 75 μm (main). Immunofluorescence images and quantification of Tenascin C, Fibronectin, Collagen XII alpha1, p-STAT3, YAP1 and DAPI. Scale bar, 75 μm and 10 μm (insert). (**b**) H&E images of PDAC tumors from patients with WT SMAD4 ($n = 10$) or mutant SMAD4 ($n = 10$); Scale

bar, 100 μm. SHG images and quantification of periductal collagen. Scale bar, 75 μm. Immunofluorescence images and quantification of Tenascin C, Fibronectin, Collagen XII alpha1, p-STAT3, YAP1 and DAPI. Scale bar, 75 μm. Results are presented as the mean +/− SEM. Subsequent statistical analysis was performed with unpaired two-sided student t-tests. (*$P < 0.05$; **$P < 0.01$, ***$P < 0.001$, ****$P < 0.0001$, “ns” not significant).